






Cite this: *Polym. Chem.*, 2019, **10**, 4459

## Effects of incorporated pyrazine on the interchain packing and photovoltaic properties of wide-bandgap D–A polymers for non-fullerene polymer solar cells†

Gururaj P. Kini,  Jun Young Choi, Sung Jae Jeon,  Il Soon Suh and Doo Kyung Moon \*

Great advancements in the photovoltaic performance of polymer solar cells (PSCs) have been achieved through the synergistic effect of aromatic and heteroaromatic units incorporated into the backbone of a conjugated polymer. However, efficient donor polymers with electron-deficient nitrogen heterocycles (N-heterocycles) for PSCs have been relatively less explored in terms of number and diversity relative to thienoacene counterparts. In this report, we investigated, for the first time, pyrazine as an acceptor core for designing wide-bandgap (WBG) polymer donors poly-{2-(5-(4,8-bis(5-(2-ethylhexyl)thiophen-2-yl)-6-methylbenzo[1,2-*b*:4,5-*b'*]dithiophen-2-yl)-4-decylthiophen-2-yl)-5-(4-decyl-5-methylthiophen-2-yl)pyrazine} (**P1**) and poly-{2-(5-(4,8-bis(5-(2-ethylhexyl)thiophen-2-yl)-6-methylbenzo[1,2-*b*:4,5-*b'*]dithiophen-2-yl)-4-(2-ethylhexyl)thiophen-2-yl)-5-(4-(2-ethylhexyl)-5-methylthiophen-2-yl)pyrazine} (**P2**) having different alkyl side chains for use in non-fullerene (NF) PSCs. These polymers demonstrated deep frontier energy levels and wide bandgaps (~2.05 eV) because of the electron-withdrawing ability of the nitrogen atoms in their pyrazine core. Additionally, they also demonstrated stronger aggregation and enhanced coplanarity because of the noncovalent interaction between the nitrogen atom of the pyrazine and adjacent thiophene units. The optimized PSCs obtained by blending **P1** and **P2** with an NF acceptor, 3,9-bis(2-methylene-(3-(1,1-dicyanomethylene)-indanone))-5,5,11,11-tetrakis(4-hexylphenyl)-dithieno[2,3-*d*:2',3'-*d'*]-*s*-indaceno[1,2-*b*:5,6-*b'*]dithiophene (ITIC) exhibited impressive efficiencies of 7.6 and 8.1%, respectively. The observed variation in the performance was studied by various characterization methods. The superior photovoltaic performance of the **P2**: ITIC blend originated from its distinctly optimized polymer design *via* regulation of its alkyl side chains, which led to downshifted frontier energy levels, a face-on orientation, and an optimum morphology compared with those of the **P1**: ITIC blend. Our findings advance the understanding of the influence of incorporated pyrazine on the optoelectronic properties of polymer donors, and this structure–relationship study provides valuable insights for designing highly efficient copolymers with N-heterocycles.

Received 10th May 2019,

Accepted 1st July 2019

DOI: 10.1039/c9py00674e

rsc.li/polymers

## 1. Introduction

Bulk heterojunction (BHJ) polymer solar cells (PSCs) comprising polymer donors and fullerene/non-fullerene (NF) acceptors have received considerable attention from both academic and industrial researchers because of their prominent benefits, which include being lightweight, semi-transparent, in-

expensive, flexible, and compatible with large-area roll-to-roll processing.<sup>1–4</sup> Traditionally, low-bandgap (LBG, bandgap < 1.7 eV)  $\pi$ -conjugated polymer (CP) donors have been preferred over wide bandgap (WBG, bandgap > 1.9 eV) CP donors for fullerene-based PSCs from the perspective of covering a broader solar absorption range.<sup>2,5–8</sup> However, since the discovery of non-fullerene fused-ring electron acceptors (NF-FREAs) with absorption in the wavelength range 600–800 nm, the synthesis of WBG CP donors with large absorption coefficients has regained attention for enabling the use of the full solar spectrum and generating more excitons.<sup>9–14</sup> Presently, a large number of NF-FREAs have been developed, thereby offering abundant opportunities to tune their absorption range, energy levels, and electronic mobility, thus enhancing power-conver-

Nano and Information Materials (NIMs) Laboratory, Department of Chemical Engineering, Konkuk University, 120, Neungdong-ro, Gwangjin-gu, Seoul 05029, Korea. E-mail: dkmoon@konkuk.ac.kr

† Electronic supplementary information (ESI) available: Experimental section, detailed synthesis of intermediates (<sup>1</sup>H and <sup>13</sup>C NMR), and additional figures and tables. See DOI: 10.1039/c9py00674e

sion efficiencies (PCEs) beyond 16%.<sup>14–19</sup> Consequently, further enhancing the PCEs of NF-PSCs necessitates the appropriate design and development of WBG CP donors with complementary absorption, tailored energy levels, an optimized BHJ morphology, and efficient charge transport when combined with NF-FREAs.

Chemical modifications such as alkyl chain variation,<sup>14,20–24</sup> insertion of a heteroaromatic acene,<sup>7,24–28</sup> or introduction of electron-withdrawing functional groups such as halogens,<sup>8,12,29–34</sup> esters,<sup>13,23,35,36</sup> or cyano<sup>37,38</sup> groups on either the donor and/or acceptor unit in alternating donor-acceptor (D-A)-based CPs are typically used as effective methods to modulate their chemical properties and optimize their performance in PSCs. Similarly, the integration of planar nitrogen-based heterocycles (N-heterocycles) with one or more electronegative nitrogen atoms into CPs has also been adopted to tailor the structural and  $\pi$ -electron behaviours of polymers without affecting their conjugation.<sup>27,28,39–43</sup> Compared with their nitrogen-free counterparts, these N-heterocycles have advantages such as (a) low-lying frontier energy levels because of the strong electronegativity of the nitrogen atom,<sup>39–42</sup> (b) minimized repulsive interactions between neighbouring molecules because of their nitrogen atoms, resulting in greater planarity,<sup>39–41</sup> and (c) enhanced crystallinity resulting from  $S^{\delta+} \cdots N^{\delta-}$  and  $N^{\delta-} \cdots H^{\delta+}$  noncovalent intermolecular interactions. In addition, (d) many copolymers of these heterocycles display absorption in the wavelength range from 300 to 650 nm, which is complementary to the absorption wavelength range of the well-known NF-FREAs.<sup>27,28,39,43</sup> Interestingly, despite the aforementioned significant properties of these N-heterocycles, only a few studies have examined their influence on the photovoltaic performance of copolymers. Recently, a few groups synthesized polymer donors using these N-heterocycles, which demonstrated impressive PCEs as high as 12%.<sup>27,28,43</sup> For example, Guo *et al.* achieved a PCE of 8.1% using a D-A polymer based on alkoxyphenyl-substituted benzo[1,2-*b*:4,5-*b'*]dithiophene (BDT) as a donor unit and bithiazole as an acceptor unit.<sup>27</sup> In another case, Peng and co-workers synthesized polymers based on alternating alkyl thienyl-BDT and 1,3,4-thiadiazole; the obtained polymers exhibited complementary absorption and well-matched energy levels with the NF-acceptor 3,9-bis(2-methylene-(3-(1,1-dicyanomethylene)-indanone))-5,5,11,11-tetrakis(4-hexylphenyl)-dithieno[2,3-*d*:2',3'-*d'*]-s-indaceno[1,2-*b*:5,6-*b'*]dithiophene (ITIC), resulting in an

impressive PCE as high as 12.8% with an extremely low energy loss of 0.48 eV.<sup>28</sup> Meanwhile, a few studies with N-incorporation also resulted in unipolar n-type transport,<sup>44</sup> and lower hole mobilities and PCEs,<sup>45,46</sup> despite the improved opto-electronic properties relative to those in cases without N-counterparts. Thus, these results indicate that optimization of the polymer structure *via* incorporation of appropriate N-heterocycles is necessary based on the type of application.

In this context, we investigated the feasibility of introducing pyrazine as an acceptor core for PSCs by synthesizing two new WBG polymers, poly-{2-(5-(4,8-bis(5-(2-ethylhexyl)thiophen-2-yl)-6-methylbenzo[1,2-*b*:4,5-*b'*]dithiophen-2-yl)-4-decylthiophen-2-yl)-5-(4-decyl-5-methylthiophen-2-yl)pyrazine} (**P1**) and poly-{2-(5-(4,8-bis(5-(2-ethylhexyl)thiophen-2-yl)-6-methylbenzo[1,2-*b*:4,5-*b'*]dithiophen-2-yl)-4-(2-ethylhexyl)thiophen-2-yl)-5-(4-(2-ethylhexyl)-5-methylthiophen-2-yl)pyrazine} (**P2**), with the well-known BDT donor (Fig. 1). Among several N-heterocycles, we deliberately selected pyrazine based on the density functional theory (DFT) results (Fig. S1†) and following considerations: first, pyrazine is a well-known heterocyclic aromatic core with symmetrically placed nitrogen atoms at the 1 and 4 positions of the benzene ring and its use in organic electronic applications has not been well explored. Second, because it contains two imine (C=N) groups, pyrazine can effectively attract electrons, resulting in a more electron-deficient unit than those in its benzene and pyridine counterparts.<sup>39</sup> Hence, it can effectively downshift the frontier energy levels and increase the open-circuit voltage ( $V_{OC}$ ) in PSCs. Third, the symmetrically positioned nitrogen can enhance the planarity of a polymer backbone by minimizing the repulsive interaction between the adjacent units *via*  $S^{\delta+} \cdots N^{\delta-}$  and/or  $N^{\delta-} \cdots H^{\delta+}$  noncovalent interactions, which is beneficial for controlling the molecular aggregation and reducing  $\pi$ - $\pi$  distances. Fourth, it has a low cost and can therefore be conveniently used in large-scale syntheses. Thus, we speculated that a pyrazine core with high polarizability and electron affinity can be used as an electron-deficient core for designing WBG polymers.

In this report, we introduce pyrazine as the acceptor core for synthesizing two new WBG polymer donors, **P1** and **P2**, which have different alkyl chains in their polymer backbones. The effects of introducing pyrazine into the CP backbone with respect to structural changes and photovoltaic performance were studied in detail through analysis of the opto-electrochemical properties, molecular orientation, charge carrier

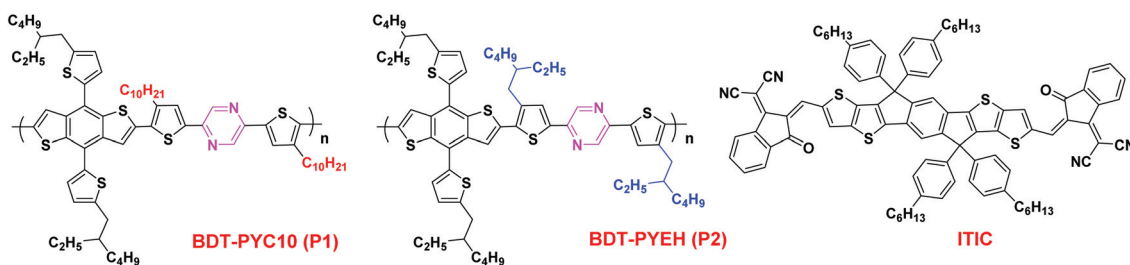


Fig. 1 Chemical structures of the BDT-Py donor polymers and the non-fullerene ITIC acceptor.

mobility, and morphology of polymer :ITIC blends. The insertion of the pyrazine units not only ensured a WBG and low-lying highest-occupied molecular orbital (HOMO) energy levels but also facilitated a coplanar geometry, promoting effective charge transport. Meanwhile, variation in the alkyl side chains also substantially affected the interchain packing and molecular orientation. In PSCs, the device based on a **P2** :ITIC blend displayed better-matched energy levels, a predominant face-on molecular orientation, and superior morphology compared to a **P1** :ITIC blend, which led to a higher PCE of 8.1% in the corresponding **P2** :ITIC-based PSC. These results indicate that the pyrazine core with significant chemical and electronic properties can be further explored in organic electronic applications.

## 2. Results and discussion

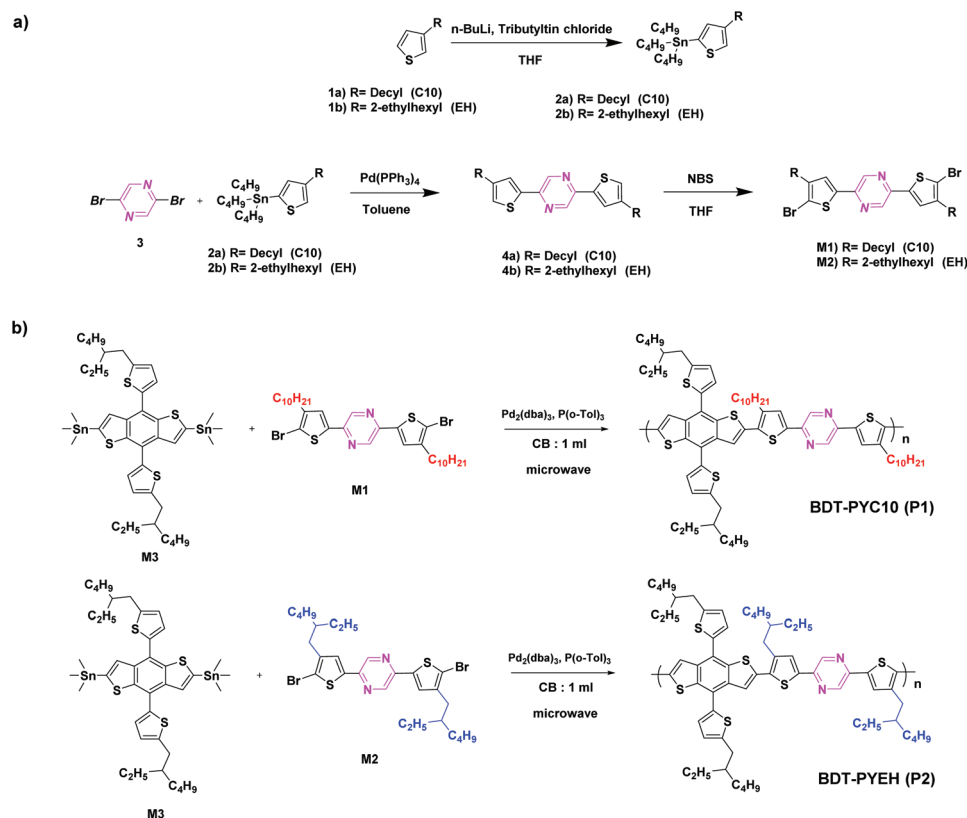
### 2.1. Synthesis and characterization

The synthetic routes of the pyrazine monomers and corresponding final polymers are outlined in Scheme 1. We synthesized the stannylated 3-alkyl-substituted thiophene monomers **2a** and **2b** by following previously reported methods.<sup>47</sup> The main pyrazine acceptor units **4a** and **4b** were prepared *via* a Stille coupling reaction between 2,5-dibromopyrazine (**3**) and the corresponding monomers **2a** and **2b**. Subsequently, the pyrazine acceptors were functionalized by bromination using *N*-bromosuccinimide, which produced the corresponding

brominated monomers **M1** and **M2**. Finally, target polymers **P1** and **P2** were synthesized *via* the microwave-assisted Stille coupling reaction between a bistannylated BDT donor (**M3**) and the corresponding brominated pyrazine acceptors (**M1** or **M2**). The detailed synthesis procedures of monomers, polymers and their characterization are given in the ESI.† Both polymers exhibited good solubility in common organic solvents such as chloroform, toluene, and chlorobenzene (CB). Using gel-permeation chromatography (GPC) with a polystyrene standard, the number-averaged molecular weights ( $M_n$ )/polydispersity indices (PDIs) of new polymers **P1** and **P2** were determined to be 44.3 kDa/2.5 and 52.6 kDa/1.6, respectively. The thermal decomposition temperature ( $T_d$ , with 5% weight loss) of **P1** and **P2** was found to be 410 and 426 °C, respectively, evaluated by thermogravimetric analysis (TGA), which indicates that these materials are sufficiently thermally stable to be used in PSCs (Fig. S2†).

### 2.2. Structural analysis by theoretical calculations

To analyze the effect of the incorporated pyrazine on the planarity and frontier molecular orbitals (FMOs) of the new polymers, molecular simulations using DFT at the B3LYP/6-31G(d) level were performed with the program Gaussian 09. To simplify the calculations, we replaced the alkyl chains on the BDT with methyl chains and carried out the calculations based on the two repeating monomeric units. First, simulations based on a polymer structure with a benzene (**P-Bn**) or pyrazine (**P1**)



**Scheme 1** Synthesis routes for pyrazine-based monomers and polymers.

acceptor core were compared to elucidate the effect of incorporated pyrazine (Fig. S3†). Noticeably, the dihedral angle between the thiophene adjacent to benzene ( $\theta_1 = 3.08^\circ$ ,  $\theta_2 = 6.11^\circ$ ) and pyrazine ( $\theta_1 = 0.45^\circ$ ,  $\theta_2 = 0.31^\circ$ ) changed substantially after introducing nitrogen atoms. Moreover, **P1** also exhibited a shorter C–C bond length between pyrazine and its adjacent thiophene ( $L_{\text{bond}}$  for **P1** = 145.59 pm;  $L_{\text{bond}}$  for **P-Bn** = 145.90 pm). The reduced dihedral angle and C–C bond length indicate enhanced planarity in the **P1** backbone, which is enabled by

intramolecular noncovalent dipole–dipole interactions such as  $S^{\delta+} \cdots N^{\delta-}$  and  $N^{\delta-} \cdots H^{\delta+}$  between the nitrogen atoms of the pyrazine and the adjacent thiophene unit.<sup>39,41</sup> Furthermore, **P1** also had lower frontier energy levels because of the high electronegativity of the nitrogen atoms, which will definitely help enhance the  $V_{\text{OC}}$  in the corresponding PSC devices.

To further investigate the effects of the side chains of polymers on their conformation and planarity, simulations based on the **P1** and **P2** structures were also performed. As shown in Fig. 2, **P1**, which has a linear decyl (C10) alkyl side chain, displayed a smaller dihedral angle ( $\theta_1 = 0.45^\circ$ ,  $\theta_2 = 0.31^\circ$ ,  $\theta_3 = 29.2^\circ$ ; and  $\theta_4 = 25.7^\circ$  for **P1**) along the polymer backbone than **P2**, which has a branched 2-ethylhexyl (EH) alkyl chain ( $\theta_1 = 0.52^\circ$ ,  $\theta_2 = 0.44^\circ$ ,  $\theta_3 = 35.7^\circ$ ; and  $\theta_4 = 35.2^\circ$  for **P2**). These results confirm the findings of previous reports that a linear alkyl chain can promote greater planarity and more ordered assemblies by minimizing distortion in the polymer backbone. On the other hand, twisting of the polymer backbone in **P2** resulted in a decrease in the HOMO and lowest unoccupied molecular orbital (LUMO) energy levels compared with those of **P1**, as calculated *via* DFT simulations. These results match well with the experimental cyclic voltammetry (CV) results discussed later in the electrochemical properties. Thus, though both polymers are assumed to be having an almost planar structure, variation in the alkyl side chains may have a substantial effect on their molecular packing and morphologies, influencing their charge-transport and electronic properties. Finally, the electrostatic potential (ESP) surface images of the polymers (Fig. 2) show an identical continuous potential along the whole backbone except the pyrazine units; this result is consistent with the nature of the pyrazine units, whose positive potential reflects their strong electron-withdrawing character attributed to the nitrogen atoms. These results provide clear evidence for the formation of a D–A-type structure and intramolecular charge transfer along the conjugated backbone of these polymers.

### 2.3. Optical and electrochemical properties

The insertion of nitrogen atoms into the copolymer backbone strongly influences the backbone planarity, molecular packing, and electron distribution. We therefore recorded the UV-vis absorption spectra of **P1** and **P2** in dilute CF solution and in the film state; the results are summarized in Table 1. As shown

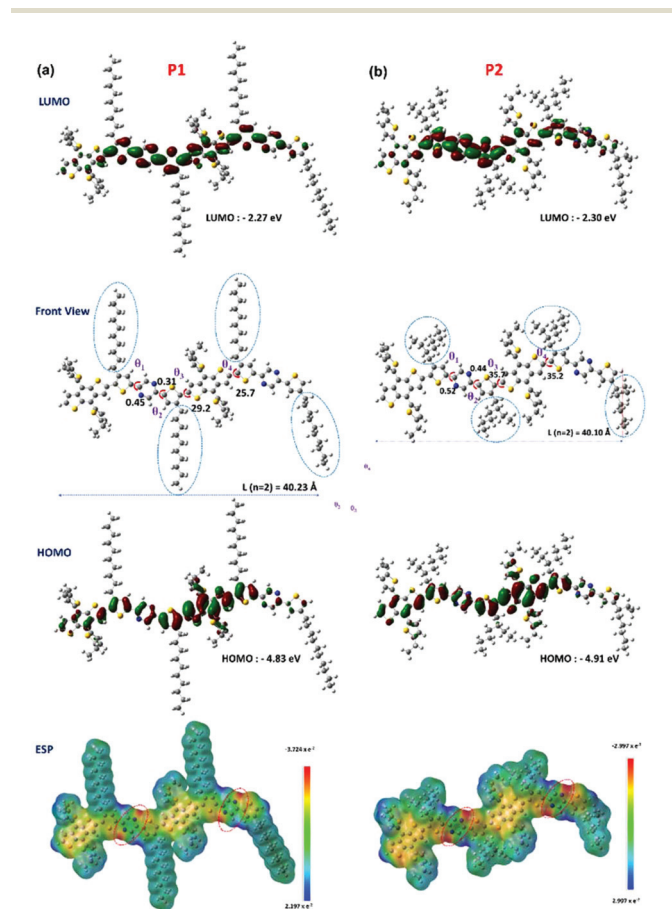


Fig. 2 Optimized geometries, isodensity surface plots, energy levels, and maps of the electrostatic potential (ESP) surfaces of dimer model molecules of the (a) **P1** and (b) **P2** polymers (calculated using the Gaussian 09 package at the B3LYP/6-31G level).

Table 1 Thermal, optical, and electrochemical properties of the new pyrazine-based polymers

Polymer	$M_n^a$ [kDa]/PDI	Thermal property	Optical properties				Electrochemical properties		
		$T_d^b$ [°C]	$\lambda_{\text{max}}$ [nm], solution	$\epsilon^c$ ( $10^4$ ) [ $M^{-1} \text{cm}^{-1}$ ]	$\lambda_{\text{max}}$ [nm], thin film	$\lambda_{\text{onset}}$ [nm], thin film	$E_g^{\text{opt}d}$ [eV]	HOMO <sup>e</sup> [eV]	LUMO <sup>e</sup> [eV]
<b>P1</b>	44.3/2.5	410	528	5.25	533, 580	635	1.95	−5.41	−3.43
<b>P2</b>	52.6/1.6	426	510	4.99	527, 573	603	2.05	−5.50	−3.48

<sup>a</sup> Number-averaged molecular weight determined by GPC. <sup>b</sup> Decomposition temperature ( $T_d$ ) was determined by TGA (with 5% weight loss). <sup>c</sup> The molar extinction coefficient of polymers at 600 nm in CF solution. <sup>d</sup> Estimated values from the UV-vis absorption edge of the thin film ( $E_g^{\text{opt}} = 1240/\lambda_{\text{onset}}$ , eV). <sup>e</sup>  $E_{\text{HOMO}}$  (or LUMO) =  $-[E_{\text{onset}}(\text{vs. Ag/AgCl}) - E_{1/2} \text{ of Fc/Fc}^+(\text{vs. Ag/AgCl})] - 4.8$  [eV] (measured  $E_{1/2}$  of Fc/Fc<sup>+</sup> (vs. Ag/AgCl) = 0.45 eV).

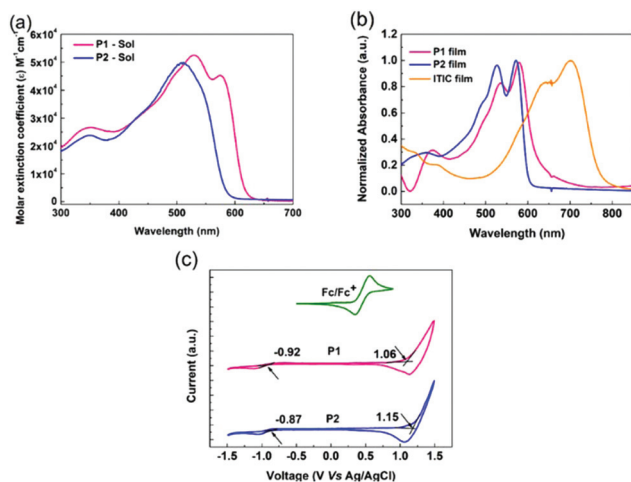


Fig. 3 Absorption spectra of the polymers **P1** and **P2** in (a) CB solutions and (b) the thin-film state; and (c) corresponding cyclic voltammograms.

in Fig. 3a and b, the spectra of both polymers exhibit distinct dual absorption bands. The high-energy absorption band at wavelengths shorter than 400 nm was attributed to the localized  $\pi$ - $\pi^*$  transitions, and a prominent absorption band at approximately 450–600 nm arises from the intramolecular charge transfer between the BDT donor and the pyrazine acceptor.<sup>36,48</sup> Compared with the spectrum of **P2**, that of **P1**, which has a linear C10 alkyl chain in its polymer backbone, showed a clear vibronic peak and a red-shifted absorption for the polymers in both the solution state and the film state, suggesting strong intermolecular  $\pi$ - $\pi$  stacking between the polymer chains. These results further substantiate the improvement in the intermolecular interactions caused by the enhancement in the structural planarity arising from the insertion of linear alkyl chains into the CP backbone.<sup>20,21</sup> Meanwhile, **P1** also exhibited a higher molar absorptivity coefficient ( $\epsilon$ ) than **P2** ( $5.25 \times 10^{-4}$  and  $49.9 \text{ M}^{-1} \text{ cm}^{-1}$  for **P1** and **P2**, respectively), which is expected to enhance light absorption and the short-circuit current density ( $J_{\text{SC}}$ ) in the corresponding PSC devices.<sup>14</sup> The absorption maxima ( $\lambda_{\text{max}}$ ) in the absorption spectra of the polymers in the film state did not substantially vary from those of the polymers in solution; however, the absorption band became broader and distinct vibronic peaks were observed in the film-state polymers. These changes suggested the formation of the more ordered molecular assemblies in the film state through enhanced  $\pi$ - $\pi$  stacking interactions. The optical bandgaps ( $E_{\text{g}}^{\text{opt}}$ ) of **P1** and **P2** were calculated to be 1.95 and 2.05 eV, respectively, which are well matched with the bandgap of the ITIC acceptor (Fig. 3b), enabling desirable complementary absorption.

The electrochemical characteristics and energy levels of the polymers were estimated from their cyclic voltammograms (Fig. 3c). The HOMO and LUMO energy levels were found to be  $-5.41/-3.43$  and  $-5.50/-3.48$  eV for **P1** and **P2**, respectively, signifying that introducing pyrazine acceptors into the polymer backbone effectively lowered the energy of the FMOs.

Notably, because of the minor distortion caused by the bulkier EH side chain in the **P2** backbone, its FMO energy levels were further lowered compared to **P1**. These trends of the electrochemical properties are consistent with the DFT results. Hence, a smaller energy offset (0.08 eV) between the HOMOs of **P2** (HOMO:  $-5.50$  eV) and ITIC (HOMO:  $-5.58$  eV) can be expected to promote charge separation and subsequently increase the  $V_{\text{OC}}$  of the corresponding PSCs.

#### 2.4. Photovoltaic properties

We estimated the photovoltaic properties of the new polymers by fabricating PSC devices with an inverted structure of indium-tin oxide (ITO)/zinc oxide (ZnO)/active layer/MoO<sub>3</sub>/Ag, where ITIC was used as an acceptor. Initially, the device fabrication conditions were optimized by varying the D-A blend ratio, solvents, and thermal annealing temperature to achieve the highest efficiency. The optimized devices were prepared by spin-coating polymer : ITIC (1.0 : 1.2, w/w) ( $22 \text{ mg mL}^{-1}$ ) in CB with 0.5 vol% 1,8-diiodooctane (DIO). Furthermore, these devices were thermally annealed at 130 °C for 10 min to optimize their nanoscale morphology and enhance their photovoltaic performance.<sup>49</sup> The detailed device structure, a band diagram of the PSC, the current density-voltage ( $J$ - $V$ ) curves, and the corresponding photovoltaic parameters of the optimized PSCs are presented in Fig. 4a-c and Table 2. Among the devices, those with polymer **P1** displayed a  $V_{\text{OC}}$  of 0.80 V, a fill factor (FF) of 58.1%, and a high  $J_{\text{SC}}$  of  $16.3 \text{ mA cm}^{-2}$ , resulting in a PCE of 7.6%. This higher  $J_{\text{SC}}$  compared with that for the devices with **P2** is consistent with the red-shifted absorption and higher absorption coefficients of **P1**. When the alkyl chain was changed from C10 to EH in **P2**, the PCE was further enhanced to 8.1%, with a  $J_{\text{SC}}$  of  $14.6 \text{ mA cm}^{-2}$ , a  $V_{\text{OC}}$  of 0.90 V, and an FF of 61.7%. Although the **P2** devices exhibit a lower  $J_{\text{SC}}$  compared with their counterpart **P1** devices, the superior efficiency of the **P2** devices stems from their substantially higher  $V_{\text{OC}}$  and FF, which are the consequences of the deeper HOMO energy levels and changes in the morphology of the **P2** : ITIC blends. The detailed device fabrication conditions for the polymers are summarized in Fig. S4 and S5 (ESI†) and Tables S1 and S2 (ESI†). Thus, the **P2** blend demonstrated an optimal trade-off between photovoltaic parameters, resulting in a relatively higher PCE. As shown in Fig. 4d, external quantum efficiency (EQE) measurements of the PSCs were performed to evaluate the fluctuation of the  $J_{\text{SC}}$  with the alkyl chain modification. Both polymers showed a broad spectral response ranging from 300 to 750 nm, and the EQE values of the **P1** blends were higher than those of the **P2** blends over the entire wavelength range. These trends are in good agreement with the effective solar absorptivity and  $J_{\text{SC}}$  values of the polymers.

#### 2.5. Molecular ordering of the polymers

Two-dimensional grazing-incidence wide-angle X-ray scattering (GIWAXS) measurements were carried out to explore the crystallinity and molecular ordering of the polymer and polymer : ITIC blends in the solid state in detail. Fig. 5 shows

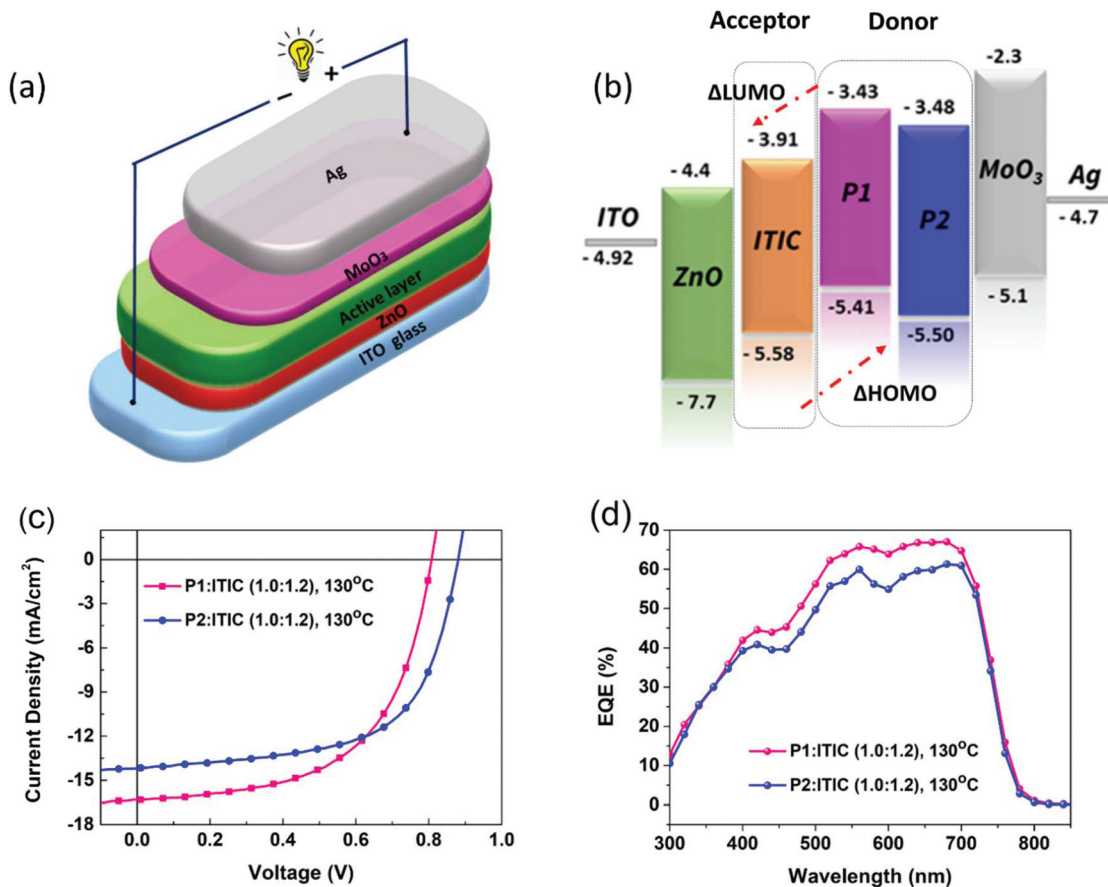


Fig. 4 (a) Cell structure and (b) energy band diagram of the polymer solar cell used in this work. (c)  $J$ - $V$  curve and (d) EQE of devices with inverted configurations based on **P1**: ITIC (1 : 1.2) and **P2**: ITIC (1 : 1.2) blend films.

Table 2 Photovoltaic performance of different polymer : ITIC (1 : 1.2) solar cell devices processed in CB with 0.5 vol% DIO under AM 1.5G illumination at 100 mW cm<sup>-2</sup>

Polymer	Annealing temperature [°C]	$V_{oc}^a$ [V]	$J_{sc}^a$ [mA cm <sup>-2</sup> ]	FF <sup>a</sup> [%]	PCE <sup>a</sup> [%]	$\mu_h^b$ [cm <sup>2</sup> V <sup>-1</sup> s <sup>-1</sup> ]
<b>P1</b>	130	0.80 (0.79 ± 0.02)	16.3 (16.2 ± 0.1)	58.1 (56.2 ± 1.9)	7.6 (7.40)	4.26 × 10 <sup>-5</sup>
<b>P2</b>	130	0.90 (0.88 ± 0.02)	14.60 (14.25 ± 0.35)	61.7 (63.1 ± 1.4)	8.1 (7.95)	5.86 × 10 <sup>-5</sup>

Device architecture: ITO/ZnO/active layer/MoO<sub>3</sub>/Ag. <sup>a</sup> The average PCE in parentheses was obtained from 6–10 independent devices. <sup>b</sup> The hole-only device had the configuration ITO/PEDOT:PSS/active layer/MoO<sub>3</sub>/Au.

the extracted GIWAXS images and the resulting in-plane (IP) and out-of-plane (OOP) line-cut profiles of a neat polymer and polymer : ITIC blends; the corresponding packing parameters are given in Table 3. The pristine **P1** and **P2** displayed scattering (100) peaks both IP and OOP, and the respective lamellar distance was found to be approximately between 19.63 to 21.66 Å. In addition, these polymers also showed intense Bragg (010) reflection peaks in both directions, suggesting that they had a bimodal orientation with respect to the substrate (*i.e.*, edge-on and face-on orientations) (Fig. 5a, b and e, f). Moreover, **P1** displayed prominent lamellar peaks up to (300) along the OOP direction and shorter  $\pi$ - $\pi$  stacking (010) in both the IP and OOP directions compared to **P2** ( $d_{010}$  IP = 3.76 and

3.90 Å for **P1** and **P2**, respectively;  $d_{010}$  OOP = 3.71 and 3.78 Å for **P1** and **P2**, respectively). These results suggest the higher crystallinity of **P1**, which originates from the presence of linear C10 chains in the **P1** structure.

After the polymers were mixed with ITIC, the (100) diffraction peaks of the **P1** blend film were retained in both the IP and OOP directions, whereas the (010) peak along the OOP direction vanished completely (Fig. 5c and e–f). Moreover, the **P1** blend still exhibited well-resolved higher-order (300) diffraction peaks along the OOP direction. These results indicate changes in the molecular ordering from mixed in pristine **P1** films to edge-on-oriented crystallites in blend films. Interestingly, in the case of the **P2**: ITIC films, although the

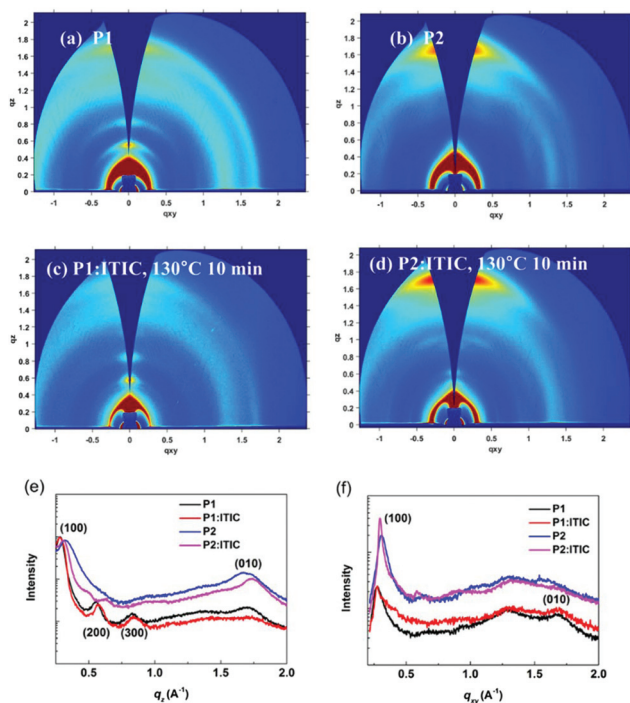


**Fig. 5** 2D-GIWAXS images of (a) pristine **P1**, (b) pristine **P2**, (c) **P1**:ITIC, and (d) **P2**:ITIC under optimized device fabrication conditions, and the corresponding (e) out-of-plane and (f) in-plane line cut profiles of the GIWAXS images.

(010) scattering peak along the IP direction disappeared completely, the (010) scattering peak at  $1.71 \text{ \AA}^{-1}$  in the OOP direction was preserved, along with the (100) peaks in both the IP and OOP directions. Furthermore, the (010) scattering peak was more pronounced than that in the pattern of the pristine film (Fig. 5d and e). These results clearly emphasize the formation of the preferential face-on orientation of the **P2** polymer in the blend film, which is beneficial for charge transport along vertical directions. Furthermore, the  $\pi$ - $\pi$  stacking distance in the **P2** blend films ( $3.67 \text{ \AA}$ ) was decreased to a greater extent than that in the **P2** pristine films ( $3.78 \text{ \AA}$ ), indicating improved crystallinity of the **P2**:ITIC films relative to **P2** films. Consequently, the face-on orientation of the **P2** blends, along with the shorter  $\pi$ - $\pi$  stacking distance, will further promote efficient exciton dissociation along the D-A interfaces, leading to an enhancement of the charge carrier mobility,  $J_{SC}$ , and the FF in PSCs.<sup>50,51</sup>

## 2.6. Hole mobility of the polymers

Since the molecular packing and nanoscale morphologies of polymer blends have a marked effect on the resulting charge-carrier properties of the PSCs, we investigated the hole mobilities ( $\mu_h$ ) of the two blends. Hole-only devices (ITO/PEDOT:PSS/active layer/MoO<sub>3</sub>/Ag) of the polymer blends were fabricated with films under optimal conditions, and the corresponding  $\mu_h$  was measured *via* the space-charge-limited current (SCLC) method.<sup>52</sup> Fig. S6† presents the resulting dark current *vs.* voltage plots of the hole only devices. The  $\mu_h$  was found to be  $4.26 \times 10^{-5}$  and  $5.86 \times 10^{-5} \text{ cm}^2 \text{ V}^{-1} \text{ s}^{-1}$  for the **P1** and **P2** blends, respectively. Thus, as noted in the discussion of the GIWAXS results, the well-ordered preferential face-on orientation and shorter  $\pi$ - $\pi$  stacking distances were the main reasons for the relatively higher hole mobility of the **P2**:ITIC blend films. Moreover, this high hole mobility must be advantageous for decreasing charge accumulation at D-A interfaces, thereby reducing charge recombination and improving the overall  $J_{SC}$ , FF, and efficiency of PSCs.<sup>7,22,53</sup>

## 2.7 Photoluminescence and morphological analysis

To elucidate the extent of exciton dissociation, we characterized the charge-transfer behavior and nanoscale morphology of the polymer blends using steady-state photoluminescence (PL), atomic force microscopy (AFM) and transmission electron microscopy (TEM) methods. Given the absorption spectra of the polymers (Fig. 3b), the PL emission spectra of the polymers and ITIC were recorded at excitation wavelengths of 550 and 700 nm, respectively, to study their electron- and hole-transfer characteristics, respectively. Under excitation wavelengths of 550 and 700 nm, the pristine polymers and ITIC showed distinct emission in the wavelength ranges 580–900 and 720–900 nm, respectively. However, in the case of the blend films, these emissions were substantially quenched at excitation wavelengths of 550 nm (76% and 73% for **P1** and **P2**, respectively) and 700 nm (72% and 85% for **P1** and **P2**, respectively) (Fig. 6a–d). Consequently, these high PL quenching efficiencies of **P2** emphasize the effective dissociation of photoinduced excitons in PSCs,<sup>54,55</sup> in good agreement with the high hole mobility and PCEs in **P2** devices.

As illustrated in Fig. 7, tapping-mode AFM and TEM measurements were conducted to correlate, in depth, the relationship among material structures, aggregation morphologies, and photovoltaic properties. The AFM images reveal

**Table 3** Packing parameters of polymers, as derived from GIWAXS measurements

Film	OOP <sup>a</sup>		IP <sup>b</sup>	
	$d$ -(100) [ $\text{\AA}$ ]/( $q$ -(100) [ $\text{\AA}^{-1}$ ])	$d$ -(010) [ $\text{\AA}$ ]/( $q$ -(010) [ $\text{\AA}^{-1}$ ])	$d$ -(100) [ $\text{\AA}$ ]/( $q$ -(100) [ $\text{\AA}^{-1}$ ])	$d$ -(010) [ $\text{\AA}$ ]/( $q$ -(010) [ $\text{\AA}^{-1}$ ])
<b>P1</b>	21.66 (0.29)	3.71 (1.69)	21.43 (0.28)	3.76 (1.67)
<b>P1</b> :ITIC	22.43 (0.280)	—	23.26 (0.27)	3.7 (1.70)
<b>P2</b>	19.63 (0.32)	3.78 (1.66)	20.26 (0.31)	3.90 (1.61)
<b>P2</b> :ITIC	20.26 (0.31)	3.67 (1.71)	21.66 (0.29)	—

<sup>a</sup> Calculation from the z-axis. <sup>b</sup> Calculation from the xy-axis.

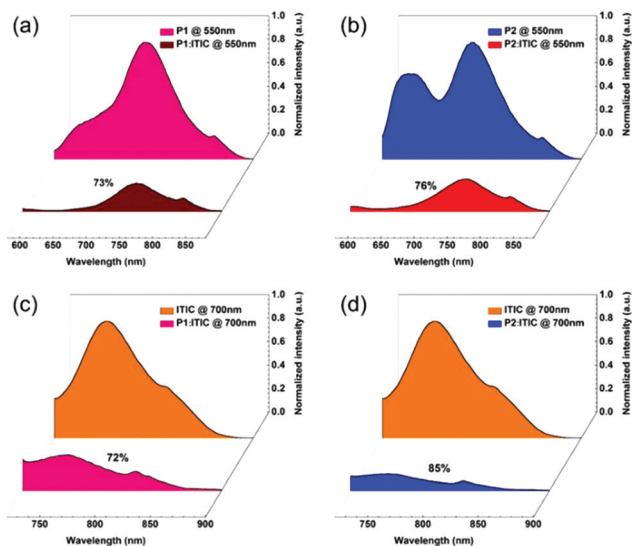


Fig. 6 (a–d) Normalized photoluminescence spectra of the polymers (excited at 550 nm) and ITIC (excited at 700 nm) films as well as the optimized polymer : ITIC blend films (1 : 1.2) (excited at 550 and 700 nm).

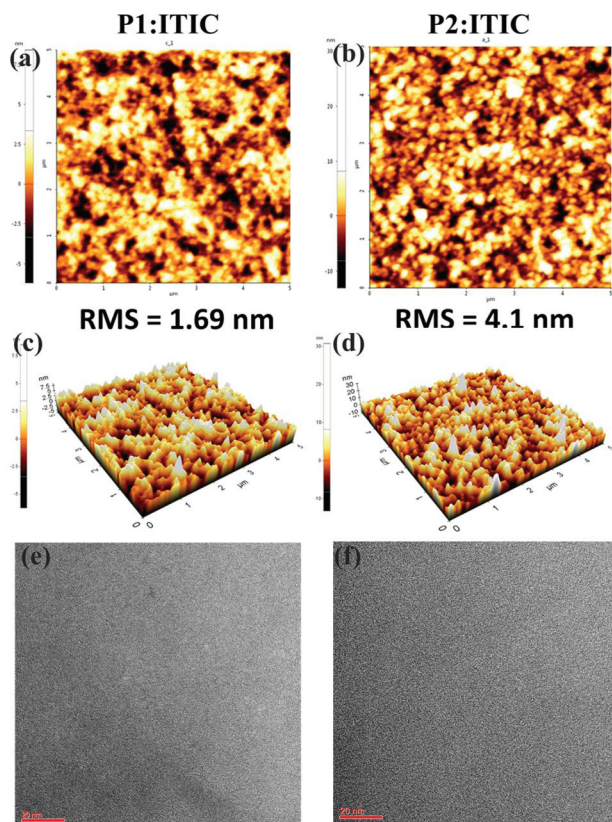


Fig. 7 AFM height, three-dimensional topography of AFM images and TEM images of the (a, c and e) **P1** : ITIC and (b, d and f) **P2** : ITIC blend films, respectively.

that though **P1** has a homogeneous and smooth morphology with a relatively small root-mean-square (RMS) roughness of 1.69 nm, it showed undesirable phase segregation with large aggregates of distinct polymer and ITIC segments (Fig. 7a). In PSCs, such phase separation processes can lead to a role of charge trap, enhancing the degree of geminate and bimolecular recombination, subsequently leading to a poor  $J_{SC}$ , FF and low efficiency.<sup>12,13,25</sup> In contrast, in the case of the **P2** blend film, these phase segregations were relatively reduced, thereby favoring continuous pathways for dissociation charge carriers (Fig. 7b). Furthermore, higher RMS roughness of the **P2** blend films (4.1 nm) further substantiated the enhancement in the crystallinity and improved molecular packing as indicated in the GIWAXS study, which would further help in improving the interfacial contact area between the active layer and interfacial layer/electrodes, hence benefitting charge collection.<sup>12,56</sup> These results were well-matched with the TEM study (Fig. 7e and f), where compared to the **P1** : ITIC film, the **P2** : ITIC blend film showed not only a well-resolved homogeneous BHJ morphology with a bicontinuous D–A interpenetrating network but also suitable domain sizes for efficient dissociation and transport of the charge carriers.<sup>22,57</sup> Thus, incorporating larger EH side chains into the **P2** backbone greatly improved its miscibility with ITIC, which in turn favored an optimal morphology with a larger D–A interface area. As a result, **P2** based PSC devices show a higher FF,  $J_{SC}$ , and efficiency than those based on **P1**.

### 3. Conclusion

In summary, by exploiting the advantages of a pyrazine core, which include high polarizability, strong electron-withdrawing ability, and low cost, we evaluated, for the first time, its feasibility as an acceptor core for PSCs by synthesizing two new WBG polymers, **P1** and **P2**, with the well-known BDT donor. Because of the strong electron-withdrawing ability of pyrazine, these polymers displayed HOMO energy levels as deep as  $-5.50$  eV, thereby giving rise to a small HOMO offset (0.08 eV) with an ITIC acceptor. Additionally, pyrazine also minimized the steric hindrance in the polymer backbone *via*  $S^{\delta+} \cdots N^{\delta-}$  and  $N^{\delta-} \cdots H^{\delta+}$  noncovalent dipole–dipole interactions, providing an alternative approach to planarization of a twisted backbone. Upon optimization of the polymer design through subtle side-chain variation, the **P2** : ITIC blend displayed well-tailored energy levels, improved miscibility, a predominant face-on molecular orientation, and a superior nanoscale morphology compared with the **P1** : ITIC blend. Consequently, the **P2** : ITIC blend films displayed superior photovoltaic performance, with a PCE of 8.1% in the corresponding PSC devices. The results of our systematic structure relationship studies of the pyrazine unit emphasize that noncovalent dipole–dipole interactions in the electron-deficient N-heterocycles can be effectively used for controlling the molecular aggregation and optoelectronic properties of the polymers and these results provide valuable



insights for designing highly efficient copolymers based on N-heterocycles.

## Conflicts of interest

There are no conflicts to declare.

## Acknowledgements

This research was supported by the New & Renewable Energy Core Technology Program (No. 20153010140030) and Human Resources program in Energy Technology (No. 20174010201540) of the Korea Institute of Energy Technology Evaluation and Planning (KETEP) grant funded by the Ministry of Trade, Industry & Energy, Republic of Korea. This research was supported by the 2019 KU Brain Pool of Konkuk University.

## References

- G. Yu, J. Gao, J. C. Hummelen, F. Wudl and A. J. Heeger, *Science*, 1995, **270**, 1789–1791.
- Y. Liu, J. Zhao, Z. Li, C. Mu, W. Ma, H. Hu, K. Jiang, H. Lin, H. Ade and H. Yan, *Nat. Commun.*, 2014, **5**, 5293.
- Y. Ma, Z. Kang and Q. Zheng, *J. Mater. Chem. A*, 2017, **5**, 1860–1872.
- Y. Lin, Y. Jin, S. Dong, W. Zheng, J. Yang, A. Liu, F. Liu, Y. Jiang, T. P. Russell, F. Zhang, F. Huang and L. Hou, *Adv. Energy Mater.*, 2018, **8**, 1701942.
- K. H. Hendriks, G. H. L. Heintges, V. S. Gevaerts, M. M. Wienk and R. A. J. Janssen, *Angew. Chem., Int. Ed.*, 2013, **52**, 8341–8344.
- J. Zhao, Y. Li, G. Yang, K. Jiang, H. Lin, H. Ade, W. Ma and H. Yan, *Nat. Energy*, 2016, **1**, 15027.
- Y. Jin, Z. Chen, S. Dong, N. Zheng, L. Ying, X.-F. Jiang, F. Liu, F. Huang and Y. Cao, *Adv. Mater.*, 2016, **28**, 9811–9818.
- K. Kawashima, T. Fukuhara, Y. Suda, Y. Suzuki, T. Koganezawa, H. Yoshida, H. Ohkita, I. Osaka and K. Takimiya, *J. Am. Chem. Soc.*, 2016, **138**, 10265–10275.
- Y. Lin and X. Zhan, *Mater. Horiz.*, 2014, **1**, 470–488.
- H. Bin, L. Gao, Z.-G. Zhang, Y. Yang, Y. Zhang, C. Zhang, S. Chen, L. Xue, C. Yang, M. Xiao and Y. Li, *Nat. Commun.*, 2016, **7**, 13651.
- W. Chen and Q. Zhang, *J. Mater. Chem. C*, 2017, **5**, 1275–1302.
- J. Yu, J. Yang, X. Zhou, S. Yu, Y. Tang, H. Wang, J. Chen, S. Zhang and X. Guo, *Macromolecules*, 2017, **50**, 8928–8937.
- D. Liu, B. Yang, B. Jang, B. Xu, S. Zhang, C. He, H. Y. Woo and J. Hou, *Energy Environ. Sci.*, 2017, **10**, 546–551.
- Z. Liao, Y. Xie, L. Chen, Y. Tan, S. Huang, Y. An, H. S. Ryu, X. Meng, X. Liao, B. Huang, Q. Xie, H. Y. Woo, Y. Sun and Y. Chen, *Adv. Funct. Mater.*, 2019, **29**, 1808828.
- C. Yan, S. Barlow, Z. Wang, H. Yan, A. K.-Y. Jen, S. R. Marder and X. Zhan, *Nat. Rev. Mater.*, 2018, **3**, 18003.
- J. Zhang, H. S. Tan, X. Guo, A. Facchetti and H. Yan, *Nat. Energy*, 2018, **3**, 720.
- H. Li, J. Wang, Y. Wang, F. Bu, W. Shen, J. Liu, L. Huang, W. Wang, L. A. Belfiore and J. Tang, *Sol. Energy Mater. Sol. Cells*, 2019, **190**, 83–97.
- A. Wadsworth, M. Moser, A. Marks, M. S. Little, N. Gasparini, C. J. Brabec, D. Baran and I. McCulloch, *Chem. Soc. Rev.*, 2019, **48**, 1596–1625.
- B. Fan, D. Zhang, M. Li, W. Zhong, Z. Zeng, L. Ying, F. Huang and Y. Cao, *Sci. China: Chem.*, 2019, **62**, 746–752.
- J. Mei and Z. Bao, *Chem. Mater.*, 2014, **26**, 604–615.
- G. P. Kini, S. K. Lee, S. Shin, S.-J. Moon, C. E. Song and J.-C. Lee, *J. Mater. Chem. A*, 2016, **4**, 18585–18597.
- G. P. Kini, Q. V. Hoang, C. E. Song, S. K. Lee, W. S. Shin, W.-W. So, M. A. Uddin, H. Y. Woo and J.-C. Lee, *Polym. Chem.*, 2017, **8**, 3622–3631.
- Y. An, X. Liao, L. Chen, J. Yin, Q. Ai, Q. Xie, B. Huang, F. Liu, A. K.-Y. Jen and Y. Chen, *Adv. Funct. Mater.*, 2018, **28**, 1706517.
- A. A. B. Alghamdi, D. C. Watters, H. Yi, S. Al-Faifi, M. S. Almeataq, D. Coles, J. Kingsley, D. G. Lidzey and A. Iraqi, *J. Mater. Chem. A*, 2013, **1**, 5165–5171.
- G. P. Kini, S. Oh, Z. Abbas, S. Rasool, M. Jahandar, C. E. Song, S. K. Lee, W. S. Shin, W.-W. So and J.-C. Lee, *ACS Appl. Mater. Interfaces*, 2017, **14**, 12617–12628.
- Y. Jin, Z. Chen, M. Xiao, J. Peng, B. Fan, L. Ying, G. Zhang, X.-F. Jiang, Q. Yin, Z. Liang, F. Huang and Y. Cao, *Adv. Energy Mater.*, 2017, **7**, 1700944.
- B. Guo, W. Li, X. Guo, X. Meng, W. Ma, M. Zhang and Y. Li, *Nano Energy*, 2017, **34**, 556–561.
- X. Xu, T. Yu, Z. Bi, W. Ma, Y. Li and Q. Peng, *Adv. Mater.*, 2018, **30**, 1703973.
- Q. Zhang, M. A. Kelly, N. Bauer and W. You, *Acc. Chem. Res.*, 2017, **50**, 2401–2409.
- G. P. Kini, J. Y. Choi, S. J. Jeon, I. S. Suh and D. K. Moon, *Polymer*, 2018, **148**, 330–338.
- Z. Ji, X. Xu, G. Zhang, Y. Li and Q. Peng, *Nano Energy*, 2017, **40**, 214–223.
- Q. Fan, Q. Zhu, Z. Xu, W. Su, J. Chen, J. Wu, X. Guo, W. Ma, M. Zhang and Y. Li, *Nano Energy*, 2018, **48**, 413–420.
- H. Chen, Z. Hu, H. Wang, L. Liu, P. Chao, J. Qu, W. Chen, A. Liu and F. He, *Joule*, 2018, **2**, 1623–1634.
- H. Zhang, H. Yao, J. Hou, J. Zhu, J. Zhang, W. Li, R. Yu, B. Gao, S. Zhang and J. Hou, *Adv. Mater.*, 2018, **30**, 1800613.
- G. E. Park, S. Choi, S. Y. Park, D. H. Lee, M. J. Cho and D. H. Choi, *Adv. Energy Mater.*, 2017, **7**, 1700566.
- G. P. Kini, J. Y. Choi, S. J. Jeon, I. S. Suh and D. K. Moon, *Dyes Pigm.*, 2019, **164**, 62–71.
- A. Casey, Y. Han, Z. Fei, A. J. P. White, T. D. Anthopoulos and M. Heeney, *J. Mater. Chem. C*, 2014, **3**, 265–275.

- 38 A. Casey, S. D. Dimitrov, P. Shakya-Tuladhar, Z. Fei, M. Nguyen, Y. Han, T. D. Anthopoulos, J. R. Durrant and M. Heeney, *Chem. Mater.*, 2016, **28**, 5110–5120.
- 39 H.-H. Cho, T. E. Kang, K.-H. Kim, H. Kang, H. J. Kim and B. J. Kim, *Macromolecules*, 2012, **45**, 6415–6423.
- 40 J. W. Jung, F. Liu, T. P. Russell and W. H. Jo, *Chem. Commun.*, 2013, **49**, 8495–8497.
- 41 B. Sun, W. Hong, Z. Yan, H. Aziz and Y. Li, *Adv. Mater.*, 2014, **26**, 2636–2642.
- 42 X. Zhang, C. Xiao, A. Zhang, F. Yang, H. Dong, Z. Wang, X. Zhan, W. Li and W. Hu, *Polym. Chem.*, 2015, **6**, 4775–4783.
- 43 B. Fan, X. Xue, X. Meng, X. Sun, L. Huo, W. Ma and Y. Sun, *J. Mater. Chem. A*, 2016, **4**, 13930–13937.
- 44 Y. Shi, H. Guo, M. Qin, J. Zhao, Y. Wang, H. Wang, Y. Wang, A. Facchetti, X. Lu and X. Guo, *Adv. Mater.*, 2018, **30**, 1705745.
- 45 X. Guo, J. Quinn, Z. Chen, H. Usta, Y. Zheng, Y. Xia, J. W. Hennek, R. P. Ortiz, T. J. Marks and A. Facchetti, *J. Am. Chem. Soc.*, 2013, **135**, 1986–1996.
- 46 X. Zhou, P. Chen, C. W. Koh, S. Chen, J. Yu, X. Zhang, Y. Tang, L. Bianchi, H. Guo, H. Y. Woo and X. Guo, *RSC Adv.*, 2018, **8**, 35724–35734.
- 47 L. Biniek, S. Fall, C. L. Chochos, D. V. Anokhin, D. A. Ivanov, N. Leclerc, P. Leveque and T. Heiser, *Macromol.*, 2010, **43**, 9779–9786.
- 48 C. E. Song, Y. J. Kim, S. R. Suranagi, G. P. Kini, S. Park, S. K. Lee, W. S. Shin, S.-J. Moon, I.-N. Kang, C. E. Park and J.-C. Lee, *ACS Appl. Mater. Interfaces*, 2016, **8**, 12940–12950.
- 49 Y. Gao, R. Zhu, Z. Wang, F. Guo, Z. Wei, Y. Yang, L. Zhao and Y. Zhang, *ACS Appl. Mater. Interfaces*, 2018, **1**, 1888–1892.
- 50 V. Vohra, K. Kawashima, T. Kakara, T. Koganezawa, I. Osaka, K. Takimiya and H. Murata, *Nat. Photonics*, 2015, **9**, 403–408.
- 51 S. Chen, H. J. Cho, J. Lee, Y. Yang, Z.-G. Zhang, Y. Li and C. Yang, *Adv. Energy Mater.*, 2017, **7**, 1701125.
- 52 G. G. Malliaras, J. R. Salem, P. J. Brock and C. Scott, *Phys. Rev.*, 1998, **58**, R13411.
- 53 Y. Li, J.-W. Lee, M. Kim, C. Lee, Y. W. Lee, B. J. Kim and H. Y. Woo, *Polym. Chem.*, 2019, **10**, 395–402.
- 54 B. Xiao, A. Tang, J. Zhang, A. Mahmood, Z. Wei and E. Zhou, *Adv. Energy Mater.*, 2017, **7**, 1602269.
- 55 B. Huang, L. Hu, L. Chen, S. Chen, M. Hu, Y. Zhou, Y. Zhang, C. Yang and Y. Chen, *J. Mater. Chem. A*, 2019, **7**, 4847–4854.
- 56 J. Yu, Y. Tang, C. Miao, K. Yang, X. Zhou, S. Yu, H. Sun, J. Huang, H. Guo, X. Guo, G. Xing and S. Zhang, *Org. Electron.*, 2019, **68**, 135–142.
- 57 J. E. Yu, S. J. Jeon, J. Y. Choi, Y. W. Han, E. J. Ko and D. K. Moon, *Small*, 2019, **15**, 1805321.